Journal of Sound and Vibration (2001) **246**(4), 653–677
doi:10.1006/jsvi.2001.3712, available online at http://www.idealibrary.com on IDEAL®

PIEZOELECTRIC ACTIVE VIBRATION CONTROL OF DAMPED SANDWICH BEAMS

M. A. TRINDADE, A. BENJEDDOU AND R. OHAYON

Structural Mechanics and Coupled Systems Laboratory, *Conservatoire National des Arts et Métiers*, 2, *rue Conté*, 75003 *Paris*, *France*. *E-mail*: *trindade@mec.puc-rio.br*

(*Received* 25 *May* 2000, *and in final form* 19 *February* 2001)

This work presents the design and analysis of the piezoelectric active control of damped sandwich beams. This is done using a specific finite element, able to handle sandwich beams with piezoelectric laminated surface layers and viscoelastic core. The piezoelectric direct and converse effects are accounted for through additional electrical degrees of freedom, condensed at the element level. The frequency dependence of the viscoelastic material properties is modelled using additional dissipative variables resulting from an anelastic displacement fields model. A complex-based modal reduction is then proposed and an equivalent real representation of the reduced-order system is constructed. The control design and performance are then evaluated using three control algorithms applied to the reduced-order model, namely, linear quadratic regulator (LQR), linear quadratic gaussian (LQG) and derivative feedback. To guarantee control feasibility and prevent piezoelectric material depoling, these algorithms are used in an iterative form to account for maximum control voltage. Parametric analyses of an actively controlled damped sandwich beam indicate that LQR controllers improve some selected modal dampings, while retaining the passive damping of uncontrolled modes. Derivative feedback controllers are less effective than an LQR one, but their well-known spillover destabilizing effects are attenuated by the increase of stability margins provided by the viscoelastic damping. It is also shown that LQG controllers may perform as well as LQR ones. Moreover, the delay effect induced by the state estimation of LQG associated with the passive attenuation lead to a damping performance similar to that of LQR with less control voltage. The parametric analyses and the comparative study of control strategies for the active control of damped sandwich beams, accounting for frequency dependence of viscoelastic material properties, are some of the originalities of this work. The others are the analysis of the LQG algorithm and the state space real representation of complex modal reduced models for hybrid piezoelectric-active viscoelastic-passive vibration control which are presented for the first time.

1. INTRODUCTION

Sandwich structures with embedded viscoelastic materials are widely used in aerospace and automotive industries due to their beneficial performance in attenuating structural vibrations. The vibratory energy is dissipated through the shear strains induced in the soft viscoelastic layer by the relative displacements of the stiffer surface layers. It is well-known that the damping performance of such structures depends on the geometrical and material properties of each layer [1]. Also, the damping performance is generally limited by geometrical and weight constraints. Consequently, to improve the damping of some selected vibration modes, one may consider active means, such as piezoelectric actuation. Indeed, piezoelectric actuators associated with appropriate control systems are known to be

0022-460X/01/390653 + 25 $35.00/0

effective to control low frequency and amplitude vibrations. The main difficulties when associating such active and passive damping mechanisms are that active controllers are generally very sensitive to system changes and the viscoelastic materials properties are frequency- and temperature-dependent. Hence, to design a sufficiently reliable and robust control system, both piezoelectric and viscoelastic materials must be well modelled.

Recently, some methods, such as fractional derivatives, anelastic displacements fields (ADF), Golla–Hughes–McTavish (GHM) and Yiu's, were proposed to model the frequency dependence of stiffness and damping properties of viscoelastically damped structures [2]. Comparison between GHM, ADF and iterative modal strain energy (MSE) models has shown that both GHM and ADF, though increasing the system dimension, are superior to MSE for time-domain analyses of highly damped structures [3]. Also, while GHM and ADF models are equivalent and lead to similar results, ADF yields to accurate damping prediction while minimizing additional degree of freedom (d.o.f.) and the number of parameters to be curve-fitted to material master curves [3]. That is why an ADF model is retained here. Although operational temperature variations can lead to high changes in the active control performance [4, 5], here, the temperature dependence is considered less important, since temperature changes are slow compared to the structural dynamics. Hence, the temperature will be considered known but constant.

Most control algorithms used in hybrid active–passive damping generally do not account for viscoelastic material property variations. Nevertheless, Baz [6] and Crassidis *et al.* [7] proposed, respectively, H_2 and H_∞ robust control algorithms to ensure the stability of an active constrained layer (ACL) treatment under viscoelastic property uncertainties due to temperature variations. Lam *et al.* [8] applied an LQR algorithm associated with the GHM frequency-dependence model to study several hybrid damping configurations. The same approach was applied by Liao and Wang [9] for the parametric analysis of ACL treatments. The drawback of the LQR control algorithm is that it requires the measurement of all state variables. This may be remedied for by considering an optimal state observer, leading to an LQG regulator, which, to the authors knowledge, has not yet been applied to hybrid damping treatments but is retained in the present work. Analysis of an ACL treatment was also made by Lesieutre and Lee [2] using the ADF model with a proportional–derivative controller. However, as in reference [9], a single-term model was considered, leading to unreal material behavior. It was shown in reference [2] that although proportional and derivative controllers suffer from spillover effects, viscoelastic damping increases their stability margins thus preventing destabilization. Friswell and Inman [4] used a positive position feedback (PPF) control algorithm associated with an iterative MSE viscoelastic model to analyze a hybrid damping treatment in thermal environments.

This work aims to present design and parametric analyses of active vibration control of damped sandwich beams. This is made using the finite element (FE) proposed in reference [10], which extends that in reference [11] to handle sandwich beams with piezoelectric laminated surface layers and viscoelastic core. The piezoelectric direct and converse effects are represented through additional electrical d.o.f., condensed at the element level. The frequency dependence of the viscoelastic material properties is modelled using the internal variables-based ADF model. Three control strategies are studied, namely LQR, LQG and derivative feedback. They are used in an iterative form to account for maximum control voltage, in order to guarantee control feasibility and prevent piezoelectric material depoling.

It is worthwhile emphasizing that the analysis of LQG algorithm and the state space real representation of complex modal reduced models for hybrid piezoelectric-active viscoelastic-passive vibration control are presented for the first time. The parametric analysis and the comparative study of control strategies for the active control of damped

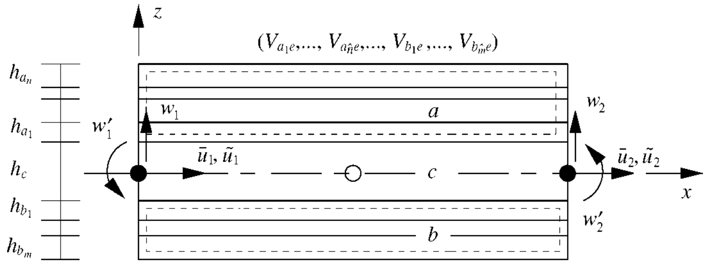

Figure 1. Piezoelectric laminated sandwich beam finite element.

sandwich beams, accounting for frequency dependence of viscoelastic materials properties, are the remaining originalities of this work.

2. SANDWICH BEAM SECOND ORDER MODEL CONSTRUCTION

An adaptive sandwich beam, composed of two laminated upper a and lower b surface layers, with, respectively, n and m elastic or piezoelectric sub-layers, and a viscoelastic core c is considered (Figure 1). The mechanical stiffnesses of the face sub-layers are composed of membrane and bending strains contributions (Euler–Bernoulli theory), while the core contains also a shear stiffness (Timoshenko theory). Since this paper focuses on the control design and performance analysis, the formulation will be only briefly presented here. Details can be found in reference [10].

2.1. FINITE-ELEMENT MODEL

The present FE model assumes Lagrange linear shape functions for the mean $\bar{u}$ and relative $\tilde{u}$ axial displacements of the surface layers and Hermite cubic ones for the transverse deflection w. Electrical difference of potentials V_{k_j} $(k = a, b; j = 1, \cdots, (\hat{n}, \hat{m}))$ are considered only in the $\hat{n}$, $\hat{m}$ piezoelectric sub-layers of the surface layer k and are assumed constant and uniform in the element (Figure 1). With these assumptions, the following elementary d.o.f. column vector $\hat{\mathbf{q}}_e$ may be written:

$$\hat{\mathbf{q}}_e = \mathrm{col}(\bar{u}_1, w_1, w_1', \tilde{u}_1, \bar{u}_2, w_2, w_2', \tilde{u}_2, V_{a_1 e}, \cdots, V_{a_{\hat{n}} e}, V_{b_1 e}, \cdots, V_{b_{\hat{m}} e}), \tag{1}$$

where $(\ )'$ implies the x-space derivative, $\bar{u} = (u_a + u_b)/2$ and $\tilde{u} = u_a - u_b$.

Discretization of the inertial, electromechanical and external virtual works of d'Alembert's variational formulation, leads to the equations of motion [10]

$$\left(\sum_k \sum_j \hat{\mathbf{M}}_{k_j}^e + \hat{\mathbf{M}}_c^e\right)\ddot{\hat{\mathbf{q}}}_e + \left(\sum_k \sum_j \hat{\mathbf{K}}_{k_j}^e + \hat{\mathbf{K}}_c^e\right)\hat{\mathbf{q}}_e = \hat{\mathbf{F}}_m^e, \quad k = a, b; j = 1, \cdots, (n, m). \tag{2}$$

where $(\ddot{\ })$ stands for the second time-derivative. $\hat{\mathbf{M}}_{k_j}^e$ and $\hat{\mathbf{M}}_c^e$ are the elementary mass matrices of the k_jth face sub-layer and core respectively. They are due to contributions related to translations in the x and z directions, and rotations. Lamination of the surface layers induce also translation–rotation coupling terms. The stiffness matrices of the face sub-layers $\hat{\mathbf{K}}_{k_j}^e$ may be decomposed into mechanical $\hat{\mathbf{K}}_{k_j m}^e$, piezoelectric $\hat{\mathbf{K}}_{k_j me}^e$ and dielectric $\hat{\mathbf{K}}_{k_j e}^e$ terms, such that

$$\hat{\mathbf{K}}_{k_j}^e = \hat{\mathbf{K}}_{k_j m}^e - \hat{\mathbf{K}}_{k_j me}^e - \hat{\mathbf{K}}_{k_j me}^{e\,\mathrm{T}} + \hat{\mathbf{K}}_{k_j e}^e, \tag{3}$$

whereas that of the core $\hat{\mathbf{K}}_c^e$ is composed only of a mechanical contribution. These matrices are defined in terms of the generalized displacements, $\bar{u}$, $\tilde{u}$ and w, in reference [10]. $\hat{\mathbf{F}}_m^e$ is a mechanical point forces vector added *a posteriori* to the discretized system.

Since the mechanical and electrical d.o.f. are coupled statically only [10] and, decomposing the element d.o.f. vector $\hat{\mathbf{q}}_e$ in mechanical d.o.f. $\mathbf{q}_e$ and unknown (sensor) $\mathbf{V}_S^e$ and applied (actuator) $\mathbf{V}_A^e$ voltages so that $\hat{\mathbf{q}}_e = \mathrm{col}(\mathbf{q}_e, \mathbf{V}_S^e, \mathbf{V}_A^e)$, system (2) may be condensed as

$$\mathbf{M}^e\ddot{\mathbf{q}}_e + [(\mathbf{K}_{fm}^e - \mathbf{K}_{fmeS}^e \mathbf{K}_{feS}^{e-1} \mathbf{K}_{fmeS}^{e\,\mathrm{T}}) + \mathbf{K}_c^e]\,\mathbf{q}_e = \mathbf{F}_m^e + \mathbf{F}_e^e, \tag{4}$$

where $\mathbf{K}_f^e$ represents the sum of all the stiffness matrices of faces sub-layers. The applied voltages $\mathbf{V}_A^e$ provide an equivalent electrical load vector $\mathbf{F}_e^e = \mathbf{K}_{fmeA}^e \mathbf{V}_A^e$, and the unknown potentials $\mathbf{V}_S^e$ are related to the mechanical d.o.f. $\mathbf{q}_e$ by $\mathbf{V}_S^e = \mathbf{K}_{feS}^{e-1} \mathbf{K}_{fmeS}^{e\,\mathrm{T}}\,\mathbf{q}_e$.

Assembling the condensed system (4) for all elements produces

$$\mathbf{M}\ddot{\mathbf{q}} + \mathbf{D}\dot{\mathbf{q}} + (\mathbf{K}_f + \mathbf{K}_c)\,\mathbf{q} = \mathbf{F}_m + \mathbf{F}_e, \tag{5}$$

where $\mathbf{D}$ is a viscous damping matrix added *a posteriori* and $\dot{\mathbf{q}}$ is a velocity vector.

2.2. SECOND ORDER AUGMENTED ADF SYSTEM

It is known that the viscoelastic material properties depend on the excitation frequency and operating temperature. To account for the frequency dependence of the viscoelastic material, Lesieutre's ADF model [2] is used. However, the operating temperature is assumed constant and the self-heating of the viscoelastic material is neglected. Temperature variation effects on viscoelastically damped beams have been investigated elsewhere [5]. By supposing a frequency-independent Poisson ratio, discretized equations of motion (5) can be rewritten in the frequency domain as

$$\{-\omega^2\mathbf{M} + \mathrm{j}\omega\mathbf{D} + [\mathbf{K}_f + G^*(\omega)\bar{\mathbf{K}}_c]\}\,\tilde{\mathbf{q}} = \tilde{\mathbf{F}}_m + \tilde{\mathbf{F}}_e, \tag{6}$$

where $G^*(\omega)$ is the complex frequency dependent shear modulus of the viscoelastic layer and $(\tilde{\ })$ stands for Fourier-transformed variables. Including n series of ADF dissipative d.o.f. $\mathbf{q}_i^d$ $(i = 1, \cdots, n)$ and re-transforming to the time domain leads to the following augmented system [3]

$$\bar{\mathbf{M}}\ddot{\bar{\mathbf{q}}} + \bar{\mathbf{D}}\dot{\bar{\mathbf{q}}} + \bar{\mathbf{K}}\bar{\mathbf{q}} = \bar{\mathbf{F}}_m + \bar{\mathbf{F}}_e, \tag{7}$$

with

$$\bar{\mathbf{M}} = \begin{bmatrix} \mathbf{M} & \mathbf{0} \\ \mathbf{0} & \mathbf{0} \end{bmatrix}, \quad \bar{\mathbf{D}} = \begin{bmatrix} \mathbf{D} & \mathbf{0} \\ \mathbf{0} & \mathbf{D}_{dd} \end{bmatrix}, \quad \bar{\mathbf{F}}_m = \begin{Bmatrix} \mathbf{F}_m \\ \mathbf{0} \end{Bmatrix}, \quad \bar{\mathbf{F}}_e = \begin{Bmatrix} \mathbf{F}_e \\ \mathbf{0} \end{Bmatrix},$$

$$\bar{\mathbf{K}} = \begin{bmatrix} \mathbf{K}_f + \mathbf{K}_c^\infty & \mathbf{K}_{qd} \\ \mathbf{K}_{qd}^{\mathrm{T}} & \mathbf{K}_{dd} \end{bmatrix}, \quad \bar{\mathbf{q}} = \mathrm{col}(\mathbf{q}, \mathbf{q}_1^d, \cdots, \mathbf{q}_n^d),$$

where

$$\mathbf{D}_{dd} = G_\infty\ \mathrm{diag}((C_1/\Omega_1)\mathbf{\Lambda} \cdots (C_n/\Omega_n)\mathbf{\Lambda}), \quad \mathbf{K}_{dd} = G_\infty \mathrm{diag}(C_1\mathbf{\Lambda} \cdots C_n\mathbf{\Lambda}),$$

$$\mathbf{K}_{qd} = [-\mathbf{K}_c^\infty\mathbf{T} \cdots -\mathbf{K}_c^\infty\mathbf{T}]$$

and $\mathbf{K}_c^\infty = G_\infty \bar{\mathbf{K}}_c$, $G_\infty = G_0(1 + \sum_i \Delta_i)$, $C_i = (1 + \sum_i \Delta_i)/\Delta_i$. Material parameters G_0 and (Δ_i, Ω_i) $(i = 1, \cdots, n)$ are evaluated by curve-fitting of the measurements of $G^*(\omega)$ [3]. $\mathbf{\Lambda}$ is a diagonal matrix of non-vanishing eigenvalues of $\mathbf{K}_c^\infty$ and $\mathbf{T}$ is the corresponding eigenvectors matrix.

3. STATE SPACE MODEL CONSTRUCTION

To apply the augmented finite-element model presented above to an optimal control design, system (7) needs to be transformed into a state space form. Therefore, a state vector $\mathbf{x}$ is formed by the augmented vector $\bar{\mathbf{q}}$ and the time derivative of the mechanical d.o.f. vector $\dot{\mathbf{q}}$. The time derivatives of the dissipative d.o.f. $\mathbf{q}_i^d$ are not considered since these variables are massless. From equation (7), this state is subjected to mechanical and electrical loads $\bar{\mathbf{F}}_m$ and $\bar{\mathbf{F}}_e$, where the latter are proportional to the voltages applied to the piezoelectric actuators.

3.1. STATE SPACE AUGMENTED ADF SYSTEM

The second order system (7) may be transformed to the following state space one:

$$\dot{\mathbf{x}} = \mathbf{A}\mathbf{x} + \mathbf{B}\mathbf{u} + \mathbf{p}, \quad \mathbf{y} = \mathbf{C}\mathbf{x}, \tag{8}$$

where each column of the control input matrix $\mathbf{B}$ represents the piezoeletric actuation loads distribution for a unitary voltage and the control input $\mathbf{u}$ is a column vector formed by the voltages $\mathbf{V}_A$ applied to the actuators. The perturbation vector $\mathbf{p}$ is the state distribution of the mechanical loads $\mathbf{F}_m$ and the output vector $\mathbf{y}$ is, generally, composed of the measured quantities, written in terms of the state vector $\mathbf{x}$ through the output matrix $\mathbf{C}$. The system dynamics are determined by the square matrix $\mathbf{A}$. Matrices and vectors of system (8) are

$$\mathbf{A} = \begin{bmatrix} \mathbf{0} & \mathbf{0} & \cdots & \mathbf{0} & \mathbf{I} \\ (\Omega_1/C_1)\mathbf{T}^{\mathrm{T}} & -\Omega_1\mathbf{I} & & \mathbf{0} & \mathbf{0} \\ \vdots & & \ddots & & \mathbf{0} \\ (\Omega_n/C_n)\mathbf{T}^{\mathrm{T}} & \mathbf{0} & & -\Omega_n\mathbf{I} & \mathbf{0} \\ -\mathbf{M}^{-1}(\mathbf{K}_f + \mathbf{K}_c^\infty) & \mathbf{M}^{-1}\mathbf{K}_c^\infty\mathbf{T} & \cdots & \mathbf{M}^{-1}\mathbf{K}_c^\infty\mathbf{T} & -\mathbf{M}^{-1}\mathbf{D} \end{bmatrix}, \quad \mathbf{x} = \begin{bmatrix} \bar{\mathbf{q}} \\ \dot{\mathbf{q}} \end{bmatrix},$$

$$\mathbf{p} = \begin{bmatrix} \mathbf{0} \\ \mathbf{M}^{-1}\mathbf{F}_m \end{bmatrix}, \quad \mathbf{B} = \begin{bmatrix} \mathbf{0} \\ \mathbf{M}^{-1}\mathbf{F}_e^* \end{bmatrix}, \quad \mathbf{C} = [\mathbf{C}_{\bar{q}} \;\; \mathbf{C}_{\dot{q}}], \quad \mathbf{u} = \mathbf{V}_A, \tag{9}$$

where $\mathbf{F}_e^*$ is the voltage factored-out electrical loads vector and $\mathbf{C}_{\bar{q}}$ and $\mathbf{C}_{\dot{q}}$ are the output matrices relative to the augmented d.o.f. vector $\bar{\mathbf{q}}$ and mechanical d.o.f. derivatives $\dot{\mathbf{q}}$, respectively. It is worthwhile noting that, although the unknown electrical d.o.f. (sensor voltages) were condensed in the FE model, they may be considered as measured output by using the relation between $\mathbf{V}_S$ and $\mathbf{q}$ to define the output matrix $\mathbf{C}$.

3.2. COMPLEX MODAL REDUCTION

The dimension of the state space system (8) is too high for use in an optimal control design. Thus, a complex-based modal reduction is applied to this system. It neglects the contributions of the viscoelastic relaxation modes and the elastic modes related to eigenfrequencies out of the frequency range considered. Hence, the eigenvalues matrix $\mathbf{\Lambda}$ and left $\mathbf{T}_l$ and right $\mathbf{T}_r$, eigenvectors of equation (8) are first evaluated from

$$\mathbf{A}\mathbf{T}_r = \mathbf{\Lambda}\mathbf{T}_r, \qquad \mathbf{A}^{\mathrm{T}}\mathbf{T}_l = \mathbf{\Lambda}\mathbf{T}_l, \tag{10}$$

so that $\mathbf{T}_l^{\mathrm{T}}\mathbf{T}_r = \mathbf{I}$, then decomposed as

$$\mathbf{\Lambda} = \begin{bmatrix} \mathbf{\Lambda}_r & \mathbf{0} & \mathbf{0} \\ \mathbf{0} & \mathbf{\Lambda}_n & \mathbf{0} \\ \mathbf{0} & \mathbf{0} & \mathbf{\Lambda}_d \end{bmatrix}, \qquad \mathbf{T}_l = [\mathbf{T}_{lr}\ \ \mathbf{T}_{ln}\ \ \mathbf{T}_{ld}], \qquad \mathbf{T}_r = [\mathbf{T}_{rr}\ \ \mathbf{T}_{rn}\ \ \mathbf{T}_{rd}], \tag{11}$$

where $\mathbf{\Lambda}_r$ is the retained elastic eigenvalues matrix and $\mathbf{T}_{lr}$ and $\mathbf{T}_{rr}$ are its left and right corresponding eigenvectors matrices respectively. $\mathbf{\Lambda}_n$ and $\mathbf{\Lambda}_d$ correspond to the neglected elastic and relaxation eigenvalues respectively. $\mathbf{T}_{ln}$, $\mathbf{T}_{rn}$, $\mathbf{T}_{ld}$ and $\mathbf{T}_{rd}$ are their corresponding left and right eigenvectors. Consequently, the state vector is approximated as $\mathbf{x} \approx \mathbf{T}_{rr}\mathbf{x}_r$ and, using equations (10) and (11), system (8) may be reduced to

$$\dot{\mathbf{x}}_r = \mathbf{\Lambda}_r\mathbf{x}_r + \mathbf{T}_{lr}^{\mathrm{T}}\mathbf{B}\mathbf{u} + \mathbf{T}_{lr}^{\mathrm{T}}\mathbf{p}, \qquad \mathbf{y} = \mathbf{C}\mathbf{T}_{rr}\mathbf{x}_r. \tag{12}$$

3.3. REAL REPRESENTATION OF THE COMPLEX MODAL REDUCED MODEL

The main disadvantage of the reduced state space system (12) is that its matrices are complex. Therefore, one may prefer to transform it to a real system before using it in the control design. Fortunately, since all overdamped (relaxation) modes were neglected, all elements of system (12) are composed of complex conjugates, such that

$$\mathbf{\Lambda}_r = \begin{bmatrix} \ddots & & & \\ & \lambda_j & & \\ & & \bar{\lambda}_j & \\ & & & \ddots \end{bmatrix}, \qquad \mathbf{T}_{lr}^{\mathrm{T}}\mathbf{B} = \begin{bmatrix} \vdots \\ \psi_j \\ \bar{\psi}_j \\ \vdots \end{bmatrix}, \qquad \mathbf{T}_{lr}^{\mathrm{T}}\mathbf{p} = \begin{bmatrix} \vdots \\ \varphi_j \\ \bar{\varphi}_j \\ \vdots \end{bmatrix}, \qquad \mathbf{C}\mathbf{T}_{rr} = [\cdots\ \ \phi_j\ \ \bar{\phi}_j\ \ \cdots], \tag{13}$$

where λ_j $(j = 1, \dots, r)$ are the retained elastic eigenvalues and $\bar{\lambda}_j$ their complex conjugates. To construct a real representation of the state space system (12), one may use a state transformation $\hat{\mathbf{x}} = \mathbf{T}_c\mathbf{x}_r$, where $\mathbf{T}_c$ is defined as [12]

$$\mathbf{T}_c = \begin{bmatrix} \ddots & & & \\ & -\mathrm{j}/2\mathrm{Im}(\lambda_j) & \mathrm{j}/2\mathrm{Im}(\lambda_j) & \\ & & & \ddots \\ \ddots & & & \\ & \frac{1}{2} - \mathrm{j}\,\frac{1}{2}(\mathrm{Re}(\lambda_j)/\mathrm{Im}(\lambda_j)) & \frac{1}{2} + \mathrm{j}\,\frac{1}{2}(\mathrm{Re}(\lambda_j)/\mathrm{Im}(\lambda_j)) & \\ & & & \ddots \end{bmatrix}, \tag{14}$$

so that the real state space system equivalent to equation (12) is

$$\dot{\hat{\mathbf{x}}} = \hat{\mathbf{A}}\hat{\mathbf{x}} + \hat{\mathbf{B}}\mathbf{u} + \hat{\mathbf{p}}, \qquad \mathbf{y} = \hat{\mathbf{C}}\hat{\mathbf{x}}. \tag{15}$$

where

$$\hat{\mathbf{A}} = \mathbf{T}_c \boldsymbol{\Lambda}_r \mathbf{T}_c^{-1} = \begin{bmatrix} & \mathbf{0} & & \mathbf{I} & \\ \ddots & & \ddots & & \\ & -|\lambda_j|^2 & & 2\mathrm{Re}(\lambda_j) & \\ & & \ddots & & \ddots \end{bmatrix},$$

$$\hat{\mathbf{B}} = \mathbf{T}_c \mathbf{T}_{lr}^{\mathrm{T}} \mathbf{B} = \begin{bmatrix} \vdots \\ \mathrm{Im}(\psi_j)/\mathrm{Im}(\lambda_j) \\ \vdots \\ \mathrm{Re}(\psi_j) + \mathrm{Im}(\psi_j)\ \mathrm{Re}(\lambda_j)/\mathrm{Im}(\lambda_j) \\ \vdots \end{bmatrix},$$

$$\hat{\mathbf{p}} = \mathbf{T}_c \mathbf{T}_{lr}^{\mathrm{T}} \mathbf{p} = \begin{bmatrix} \vdots \\ \mathrm{Im}(\varphi_j)/\mathrm{Im}(\lambda_j) \\ \vdots \\ \mathrm{Re}(\varphi_j) + \mathrm{Im}(\varphi_j)\ \mathrm{Re}(\lambda_j)/\mathrm{Im}(\lambda_j) \\ \vdots \end{bmatrix},$$

$$\hat{\mathbf{C}} = \mathbf{C}\mathbf{T}_{rr}\mathbf{T}_c^{-1} = [\cdots\ -2[\mathrm{Re}(\phi_j)\,\mathrm{Re}(\lambda_j) + \mathrm{Im}(\phi_j)\,\mathrm{Im}(\lambda_j)] \cdots 2\mathrm{Re}(\phi_j)\ \cdots].$$

It is clear that the eigenvalues of the real matrix $\hat{\mathbf{A}}$ are exactly the elements of $\boldsymbol{\Lambda}_r$. In form (15), the new state variables $\hat{\mathbf{x}}$ represent the modal displacements and velocities.

4. CONTROL DESIGN

The analysis of the LQR algorithm for the hybrid piezoelectric-active viscoelastic-passive vibration control was presented in previous papers [3, 10]. Here, the objective is to analyze and compare the hybrid damping performance of other control algorithms, which is done for the first time. Hence, in this section, three control strategies are briefly presented, namely LQR, LQG and derivative feedback. It is clear that, for practical applications, these algorithms must be used in an iterative form to account for maximum control voltage, since piezoelectric actuators can be depoled by high oscillating voltages.

4.1. CONSTRAINED OPTIMAL CONTROL STRATEGY

The LQR optimal control algorithm consists of minimizing the functional

$$J = \tfrac{1}{2}\int_0^\infty (\hat{\mathbf{x}}^{\mathrm{T}}\mathbf{Q}\hat{\mathbf{x}} + \mathbf{u}^{\mathrm{T}}\mathbf{R}\mathbf{u})\,\mathrm{d}t. \tag{16}$$

subjected to linear constraints (15). This minimization yields a linear full-state feedback control law $\mathbf{u} = -\mathbf{K}_g\hat{\mathbf{x}}$, where the control gain matrix $\mathbf{K}_g = \mathbf{R}^{-1}\hat{\mathbf{B}}^{\mathrm{T}}\mathbf{P}$ is evaluated by solving for $\mathbf{P}$ the following algebraic Riccati equation

$$\hat{\mathbf{A}}^{\mathrm{T}}\mathbf{P} + \mathbf{P}\hat{\mathbf{A}} - \mathbf{P}\hat{\mathbf{B}}\mathbf{R}^{-1}\hat{\mathbf{B}}^{\mathrm{T}}\mathbf{P} + \mathbf{Q} = \mathbf{0}. \tag{17}$$

Evidently, the performance of this controller depends on the state $\mathbf{Q}$ and input $\mathbf{R}$ weight matrices. While $\mathbf{Q}$ defines the relative weight of each state variable, $\mathbf{R}$ defines the relative weight of each actuator voltage. The latter may then be adjusted to limit the maximum voltage. The iterative algorithm developed and presented in reference [5] is used here to perform such fitting automatically. However, the voltage limitation leads to a perturbation-dependent performance of the controller [5].

4.2. OPTIMAL FULL-STATE OBSERVER AND CONTROLLER

The full-state feedback control using the LQR algorithm is clearly only feasible when all state variables can be measured. Since, generally, this is not the case, one must estimate the state variables using the measured ones. For that, let one define the Luenberger state observer [13] as

$$\dot{\tilde{\mathbf{x}}} = \hat{\mathbf{A}}\tilde{\mathbf{x}} + \hat{\mathbf{B}}\mathbf{u} + \hat{\mathbf{p}} + \mathbf{K}_e(\mathbf{y} - \hat{\mathbf{C}}\tilde{\mathbf{x}}), \qquad \tilde{\mathbf{x}}(\mathbf{0}) = \mathbf{0}, \tag{18}$$

where $\tilde{\mathbf{x}}$ is the estimated state vector and $\mathbf{K}_e$ is the observer gain matrix. The Luenberger observer simulates real system (15) and penalizes the difference between the measured output $\mathbf{y}$ and the estimated output $\hat{\mathbf{C}}\tilde{\mathbf{x}}$. Input $\mathbf{w}$ and output $\mathbf{v}$ noise contributions are added, respectively, to state excitation $\mathbf{p}$ and output measurement $\mathbf{y}$ in equation (15). Hence, replacing $\mathbf{y} = \hat{\mathbf{C}}\hat{\mathbf{x}} + \mathbf{v}$ in equation (18), then subtracting the resulting equation from the state space system (15a), with added noise term $\mathbf{w}$, leads to

$$\dot{\mathbf{e}} = (\hat{\mathbf{A}} - \mathbf{K}_e\hat{\mathbf{C}})\mathbf{e} + \mathbf{w} - \mathbf{K}_e\mathbf{v}, \tag{19}$$

where $\mathbf{e} = \hat{\mathbf{x}} - \tilde{\mathbf{x}}$ states for the observation error and has initial value $\mathbf{e}(\mathbf{0}) = \hat{\mathbf{x}}(\mathbf{0})$. One notices, from equation (19), that the observation error $\mathbf{e}$ is asymptotically stable if the eigenvalues of $\hat{\mathbf{A}} - \mathbf{K}_e\hat{\mathbf{C}}$, also named observer poles, have negative real parts. It can be also shown [13] that if the system is completely observable, one might place the observer poles arbitrarily far in the complex left mid-plan to obtain fast error convergence, thus fast state estimation. However, this yields to large $\mathbf{K}_e$ elements that may amplify the measurement noise $\mathbf{v}$. Hence, a compromise between noise amplification and state estimation velocity must be found.

The well-known Kalman–Bucy Filter (KBF) allows the observer to evaluate gain matrix $\mathbf{K}_e$ for white input $\mathbf{w}$ and output $\mathbf{v}$ noises [13]; that is, for expectations $E[\mathbf{w}] = \mathbf{0}$ and $E[\mathbf{v}] = \mathbf{0}$. Then, the optimal gain $\mathbf{K}_e$ is obtained through minimization of the following quadratic cost function

$$J_e = \mathbf{h}^{\mathrm{T}}\mathbf{P}_e\mathbf{h} \tag{20}$$

for any arbitrary vector $\mathbf{h}$ and $\mathbf{P}_e = E[\mathbf{e}\mathbf{e}^{\mathrm{T}}]$. The optimal observer covariance matrix $\mathbf{P}_e$ is the solution of the following algebraic Riccati equation

$$\hat{\mathbf{A}}\mathbf{P}_e + \mathbf{P}_e\hat{\mathbf{A}}^{\mathrm{T}} - \mathbf{P}_e\hat{\mathbf{C}}^{\mathrm{T}}\mathbf{V}^{-1}\hat{\mathbf{C}}\mathbf{P}_e + \mathbf{W} = \mathbf{0}. \tag{21}$$

Here $\mathbf{W}$ and $\mathbf{V}$ are the input $\mathbf{w}$ and output $\mathbf{v}$ noises covariance matrices. The optimal gain $\mathbf{K}_e$ is then defined as

$$\mathbf{K}_e = \mathbf{P}_e\hat{\mathbf{C}}^{\mathrm{T}}\mathbf{V}^{-1}. \tag{22}$$

From equation (19), one notices that the matrix **V** penalizes the observer gain to limit the amplification of the output noise through the term $\mathbf{K}_e\mathbf{v}$. Whereas, for noisy inputs, the matrix **W** increases the observer gain to damp quickly the error this noise produces.

Assembling system (15a), with added noise terms and for $\mathbf{u} = -\mathbf{K}_g\tilde{\mathbf{x}}$, and equation (19) yields the coupled system

$$\begin{Bmatrix} \dot{\hat{\mathbf{x}}} \\ \dot{\mathbf{e}} \end{Bmatrix} = \begin{bmatrix} \hat{\mathbf{A}} - \hat{\mathbf{B}}\mathbf{K}_g & \hat{\mathbf{B}}\mathbf{K}_g \\ \mathbf{0} & \hat{\mathbf{A}} - \mathbf{K}_e\hat{\mathbf{C}} \end{bmatrix} \begin{Bmatrix} \hat{\mathbf{x}} \\ \mathbf{e} \end{Bmatrix} + \begin{Bmatrix} \hat{\mathbf{p}} \\ \mathbf{0} \end{Bmatrix} + \begin{bmatrix} \mathbf{I} & \mathbf{0} \\ \mathbf{I} & -\mathbf{K}_e \end{bmatrix} \begin{Bmatrix} \mathbf{w} \\ \mathbf{v} \end{Bmatrix}, \tag{23}$$

where equation (15b) is still valid. This combination of an optimal LQR controller with a KBF optimal observer is known as the LQG algorithm. Owing to the block triangular form of this system, one may design the LQR optimal controller alone, then use it to design the optimal observer. However, the stability of coupled system (23) is evidently dependent on the stability of both sub-systems.

4.3. DERIVATIVE FEEDBACK CONTROLLER

An alternative to the complexities involved in the calculations of an optimal observer and controller is a simple derivative feedback. Considering that the output vector **y** can be measured, one may feed it back after amplification to the actuator as a control voltage $\mathbf{u} = -K_d\mathbf{y}$. Notice that the output vector is a linear combination of the state variables ($\mathbf{y} = \hat{\mathbf{C}}\hat{\mathbf{x}}$), which are themselves a combination of the finite-element model variables **q** and their time derivatives. Hence, using the decomposition of the output matrix **C** into $\mathbf{C}_{\bar{q}}$ and $\mathbf{C}_{\dot{q}}$ (cf. equation (9)), leads to

$$\mathbf{y} = \hat{\mathbf{C}}\hat{\mathbf{x}} = \hat{\mathbf{C}}\mathbf{T}_c\mathbf{T}_{lr}^{\mathrm{T}}\mathbf{x} = \mathbf{C}_{\bar{q}}\bar{\mathbf{q}} + \mathbf{C}_{\dot{q}}\dot{\mathbf{q}}. \tag{24}$$

To get a derivative control, the output is set to a combination of time derivatives only, so that $\mathbf{C}_{\bar{q}} = \mathbf{0}$. Transforming back the state space system (8) to a second order one, using equation (9) together with $\mathbf{u} = -K_d\mathbf{C}_{\dot{q}}\dot{\mathbf{q}}$, one notices that such a derivative control is equivalent to the substitution, in system (7), of the following electrical loads vector

$$\mathbf{F}_e = -\mathbf{F}_e^* K_d \mathbf{C}_{\dot{q}}\dot{\mathbf{q}}. \tag{25}$$

Consequently, when moved to the l.h.s. of equation (7), this leads to a modification of its damping matrix which becomes

$$\bar{\mathbf{D}}^* = \begin{bmatrix} \mathbf{D} + K_d\mathbf{F}_e^*\mathbf{C}_{\dot{q}} & \mathbf{0} \\ \mathbf{0} & \mathbf{D}_{dd} \end{bmatrix}. \tag{26}$$

It is clear that the positive definiteness of the additional damping matrix $K_d\mathbf{F}_e^*\mathbf{C}_{\dot{q}}$, provided by the active controller, is a consequence of the relation between input $\mathbf{F}_e^*$ and output $\mathbf{C}_{\dot{q}}$ vectors. Since $\mathbf{F}_e^*$ and $\mathbf{C}_{\dot{q}}$ are relative to the mechanical d.o.f. that are affected by the piezoelectric actuator and those that contribute to the output, respectively, the increase of modal damping is dependent on the relative positions of the piezoelectric sensor and actuator.

5. NUMERICAL RESULTS

In this section, the piezoelectric active control of a cantilever sandwich beam, passively damped by its viscoelastic core, is studied. Figure 2 shows the configuration of the cantilever

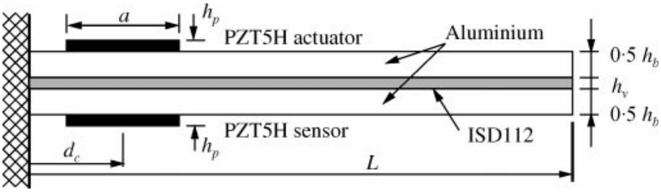

Figure 2. Cantilever sandwich beam with bonded piezoelectric actuator and sensor.

TABLE 1

Properties of the damped sandwich beam with bonded piezoelectric patches

	Aluminum	PZT5H	ISD112
Modified Young's modulus (GPa)	79·8	65·5	various
Density (kg m^{-3})	2690	7500	1600
Modified e_{31} constant (C m^{-2})	—	− 23·2	—
Modified e_{33} constant (F m^{-1})	—	$1{\cdot}54 \times 10^{-8}$	—
Length, L (mm)	280	$a = 50$ ($d_c = 35$)	280
Thickness, h_b (mm)	3	$h_p = 0{\cdot}5$	$h_v = 0{\cdot}1$
Width, b (mm)	25	25	25

sandwich beam. Its material and geometrical properties are given in Table 1. The objective is to use the piezoelectric patches to increase actively the damping of the first bending modes of the passively damped beam. First, a parametric analysis of the active and passive control performances, using LQR control algorithm, is performed to find the optimal geometric configuration. Then, derivative feedback and LQG controllers are applied to this optimal configuration to compare the three controllers' performances.

The frequency dependence, in the range 20–5000 Hz, of the ISD112 viscoelastic material at 27°C is represented by a three-series ADF model, with the parameters. $G_0 = 0{\cdot}50$ MPa, $\Delta = [0{\cdot}746,\ 3{\cdot}265,\ 43{\cdot}284]$ and $\Omega = [468{\cdot}7,\ 4742{\cdot}4,\ 71532{\cdot}5]$ rad/s. These optimal ADF parameters yield a good approximation to the measured material master curves in the frequency range of interest as shown in Figure 3. Indeed, both elastic modulus G' and loss factor η evaluated using ADF parameters (dashed lines) match well with measured ones (solid lines). The model reduction presented previously is performed by keeping the first five bending eigenmodes of the damped sandwich beam. Since the corresponding complex reduced model has been validated in a previous paper [10], the focus here is on its equivalent real representation which is used for the first time. However, from section 3.3, one notices that their dynamical behavior must be equivalent. Figure 4 shows the frequency response function between the perturbation force and piezoelectric sensor using the full model (8) and the real reduced-order model (15). One notices that responses match well in the frequency range of interest.

5.1. LQR OPTIMAL CONTROL OF THE SANDWICH DAMPED BEAM

To improve actively the damping of the first three bending modes, the piezoelectric actuator bonded on the upper surface of the sandwich beam is combined to an iterative LQR algorithm [5], with parameters $\mathbf{Q} = \mathrm{diag}(1, 1, 1, 0, \cdots, 0)$ and $\mathbf{R} = \gamma\mathbf{I}$. The factor γ is

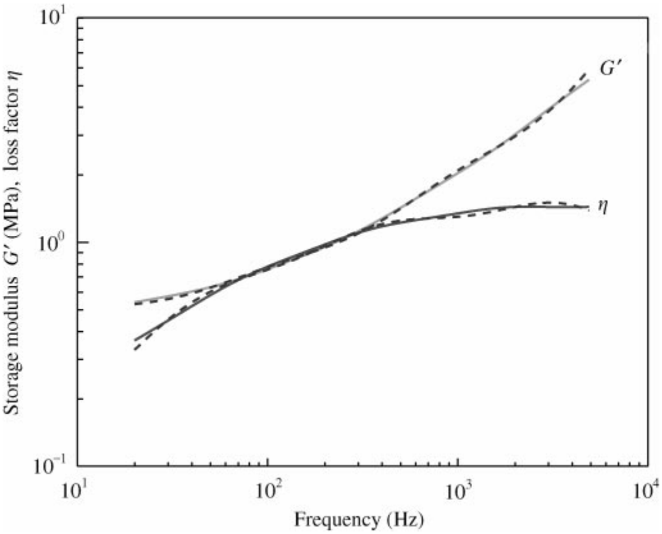

Figure 3. Elastic modulus G' and loss factor η of 3M ISD112 viscoelastic material evaluated using three series of ADF parameters (dashed lines) and measured ones (solid lines).

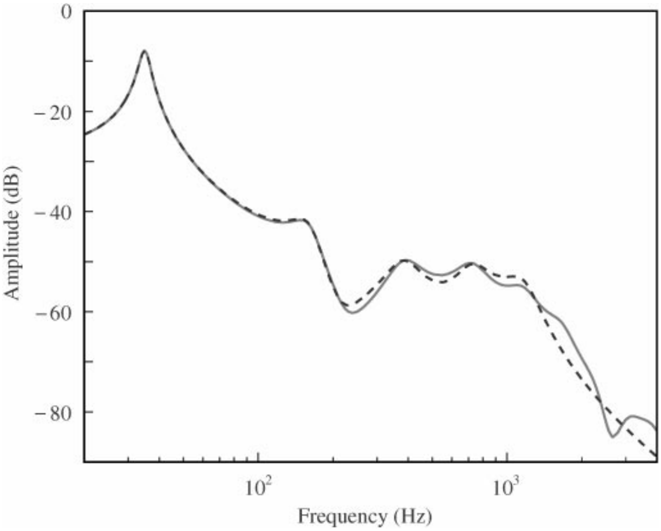

Figure 4. Frequency response function between the perturbation force and piezoelectric sensor using the full model (solid lines) and real reduced-order model (dashed lines).

evaluated automatically in the LQR algorithm to limit the control voltage to 250 V, leading to a maximum electrical field of 500 V/mm in the piezoelectric actuator. The piezoelectric sensor, although not used in this case, is preserved for future comparisons. A perturbation transverse force is applied to the beam tip, whose deflection is measured and restrained to 1·5 mm.

A parametric analysis of the passive damping, provided by the viscoelastic layer, and hybrid damping, which is the passive one increased by the active controller, is performed. This is achieved by varying the piezoelectric patch length in the range 20–70 mm and the

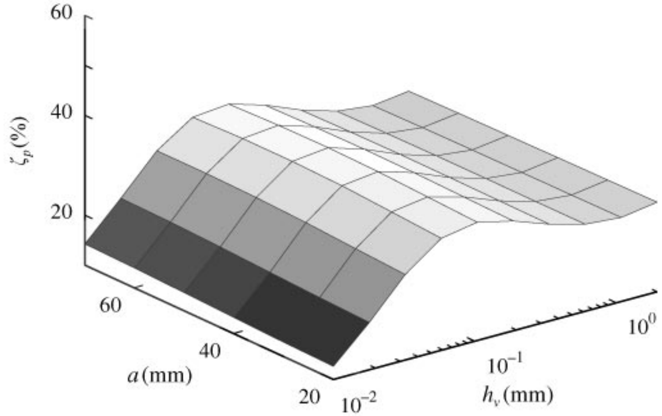

Figure 5. Sum of the first three open-loop modal damping factors of the sandwich beam.

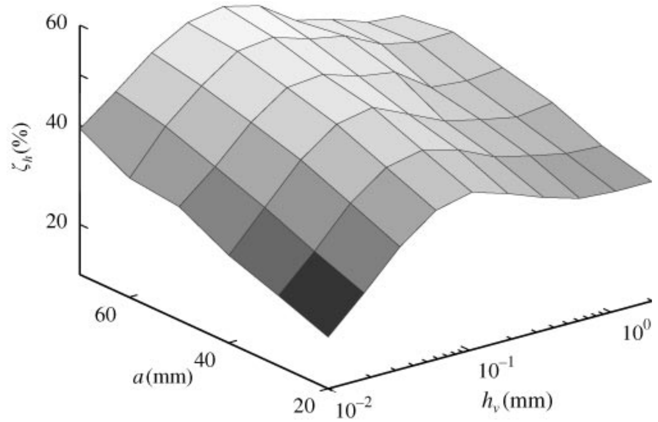

Figure 6. Sum of the first three closed-loop modal damping factors of the sandwich beam.

viscoelastic core thickness in the range 0·01–2 mm. To guarantee adequate levels of damping for the first three bending modes, parameters optimization is based on the sum of these three modal damping factors. Figure 5 shows that increase of piezoelectric patch length has little effect in passive damping. In fact, due to an augmentation of the surface layer stiffness, small improvement in the second and third modal damping is obtained. However, this does not enhance the passive damping of the first mode and is not observable in Figure 5. This figure shows also that the passive damping is optimal for relatively thin viscoelastic layers ($h_v = 0{\cdot}1$ mm) and decreases for both very thin ($h_v = 0{\cdot}01$ mm) and thick ($h_v = 2$ mm) layers.

The sum of the first three closed-loop modal damping factors of the sandwich beam is presented in Figure 6 for several piezoelectric patch lengths and viscoelastic core thicknesses. It appears that the hybrid damping performance is optimal for long actuators ($a = 70$ mm) and relatively thin viscoelastic cores ($h_v = 0{\cdot}1$ mm), although it is adequately effective in the range $40 < a < 70$ mm and $0{\cdot}1 < h_v < 2$ mm. Nevertheless, the damping gain provided by the active controller, defined as $\zeta_a = \zeta_h/\zeta_p - 1$, is optimal for very thin viscoelastic cores, as shown in Figure 7. This is mainly due to the fact that passive damping

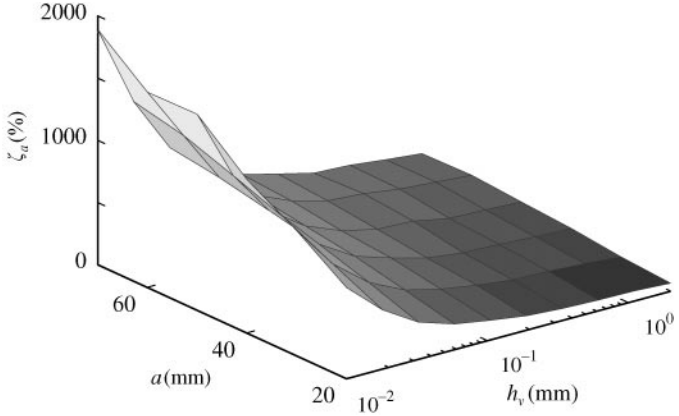

Figure 7. Sum of the first three damping gains provided by the piezoelectric actuator.

Table 2

Optimal results of hybrid control of damped sandwich beam

	ζ_1 (%)	ζ_2 (%)	ζ_3 (%)	ζ_4 (%)	ζ_5 (%)	t_s (s)	$\mathbf{y}_{max}$ (mm)
Passive	5·01	13·36	16·17	15·94	15·57	0·60	1·50
Hybrid	24·85	13·63	16·36	15·94	15.57	0·10	1·07

is not effective in that case. However, this quantity gives a good measure of the advantage of considering an active controller in addition to a passive damping.

To yield both hybrid and passive performant damping properties, optimal parameters are set to maximize the sum of open- and closed-loop damping factors, which are already the sum of the corresponding first three modal dampings. The optimal damping performances of the open- and closed-loop sandwich beam are presented in Table 2. The latter shows that, for optimal parameters, that is for $a = 70$ mm and $h_v = 0{\cdot}1$ mm, the first mode damping is increased by 400% and the non-controlled fourth and fifth modes are not excited by the controller. The damping factors of the second and third modes are just slightly improved by the active control.

For the optimal parameters, frequency- and time-domain responses of the sandwich beam are evaluated in both open- and closed-loops. Hence, the frequency response function between the transverse excitation force and the tip deflection of the beam is evaluated and shown in Figure 8. It shows that the active controller produces a decrease of 14 dB in the amplitude of the first resonance, compared to the passive case. Moreover, it preserves or enhances the passive damping of the other modes. It should be noticed, in Figure 8, that the last four modes considered are highly damped, as also shown in Table 2, so that they are less observable. This passive damping performance prevent instabilities due to spillover.

The open- and closed-loop transient responses of the sandwich beam tip deflection are presented in Figure 9. It should be noticed that the closed-loop response settles much faster than the open-loop one. In fact, as shown in Table 2, the settling time t_s and maximum amplitude $\mathbf{y}_{max}$ of the closed-loop beam transient response are reduced by 83% and 29%, respectively, compared to those in the open loop. The control voltage applied to the piezoelectric actuator to obtain this performance is shown in Figure 10. It is clear that the control voltage subsides as fast as the closed-loop response. Also, as required by the iterative optimal control algorithm, the control voltage is limited to 250 V.

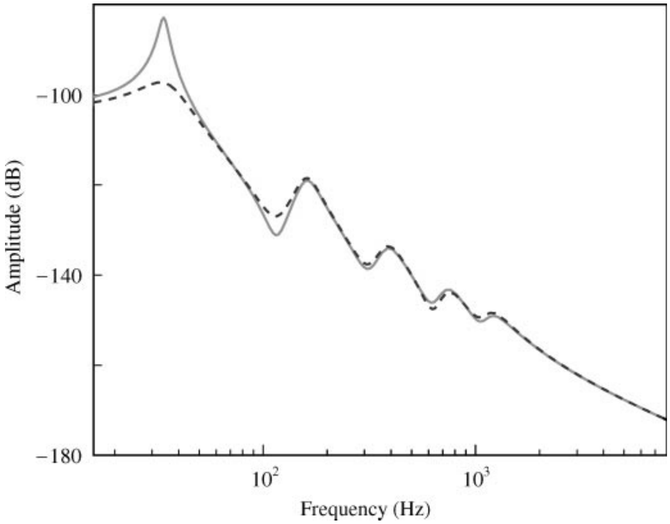

Figure 8. Open- and closed-loop FRF of the sandwich beam, measured by the tip deflection and loaded by the perturbation transverse force, for optimal parameters $a = 70$ mm and $h_v = 0{\cdot}1$ mm: —, passive; - - -, hybrid.

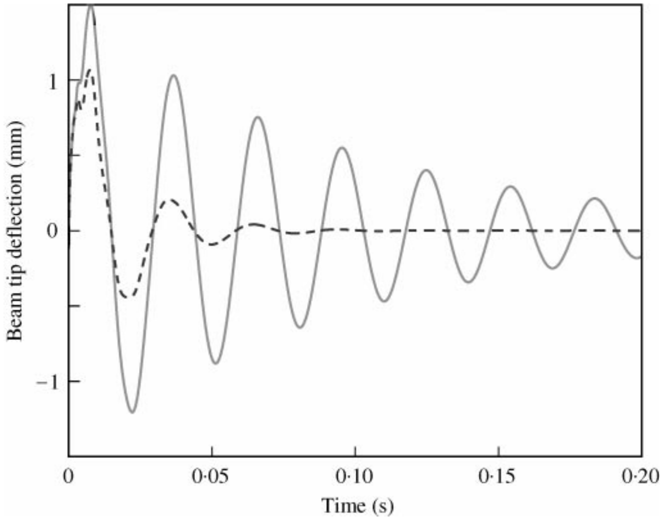

Figure 9. Open- and closed-loop transient responses of the sandwich beam tip deflection for optimal parameters $a = 70$ mm and $h_v = 0{\cdot}1$ mm: —, passive; - - -, hybrid.

5.2. DERIVATIVE CONTROL OF THE OPTIMAL BEAM CONFIGURATION

The main drawback of the LQR algorithm is the need to measure all state variables to construct the full-state feedback. Thus, in this section, the much simpler approach of derivative feedback is applied to the optimal case of the cantilever sandwich beam with bonded piezoelectric actuator and sensor of Figure 2, that is for $a = 70$ mm and $h_v = 0{\cdot}1$ mm. To this end, two measured outputs are considered, namely the time-derivative of the beam tip deflection $\dot{w}_L$ and that of the voltage $\dot{V}_S$ of the piezoelectric sensor bonded on the bottom surface of the sandwich beam (Figure 2).

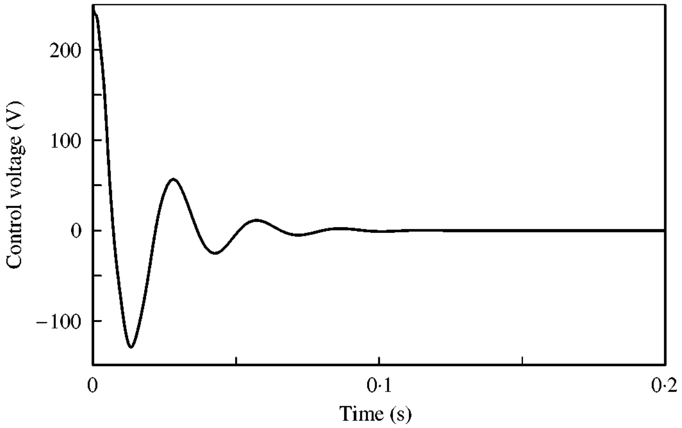

Figure 10. Piezoelectric actuator control voltage for optimal parameters $a = 70$ mm and $h_v = 0{\cdot}1$ mm.

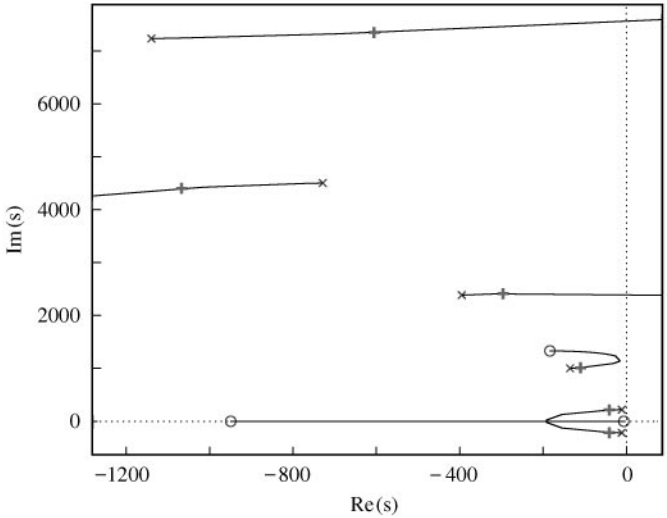

Figure 11. Root locus between the velocity sensor on the beam tip and the piezoelectric actuator (open-loop poles, ×, and zeros, ○, and closed-loop poles, +, for $K_d = 605$).

5.2.1. *Tip deflection velocity feedback*

First, a control voltage proportional to the time derivative of the sandwich beam tip deflection $\dot{w}_L$ is considered, such that $V_A = -K_d\dot{w}_L$. It is clear from equation (26) that higher control gains lead to higher additional damping factors and, provided that the actuator/sensor combination increases the damping of a given set of modes, the total damping will increase with the control gain. However, since the control voltage is proportional to the control gain, it is also clear that large control gains yield to high control voltages. Hence, these should be limited to the maximum voltage that can be applied to the piezoelectric actuator.

Figure 11 shows the root locus between a point velocity sensor on the tip of the beam and the piezoelectric actuator. In this figure, the increase of the control gain K_d moves the open-loop poles, ×, toward the open-loop zeros, ○. Moreover, the modal damping Im(s)/Re(s) increases when the poles move away from the imaginary axis Re(s) = 0.

Consequently, from Figure 11, one notices that this control law allows one to increase greatly the first and fourth modal dampings and, for large control gains, that of the second mode. However, it reduces the third and fifth modal dampings, for all control gains, such that their destabilization is only prevented by their passive damping. Thus, one notices that the viscoelastic passive damping increases the stability margins of the modes excited by the active control. The closed-loop poles, +, for the maximum control gain considered ($K_d = 605$) are also presented in Figure 11. The control gain K_d is limited to prevent voltage saturation in the piezoelectric actuator (in this case, 250 V). One notices that, although from Figure 11 this control law may improve the second modal damping, the voltage limitation leads to its decrease.

The responses of the first five bending modes, in the frequency domain, are presented in Figure 12, for three control gains 137, 302 and 605. One notices that, as observed previously, the first and fourth modes are well damped, compared to the open-loop response ($K_d = 0$), whereas the other modes are excited for the three control gains, as expected from the analysis of Figure 11. The additional modal dampings provided by the active controller are presented in Table 3 (Gain $\dot{w}_L$). This table shows that the modes 2, 3 and 5 are excited by the active controller. That is, their modal dampings are reduced compared to the passive damping. However, as observed also in Figure 11, the passive damping due to the

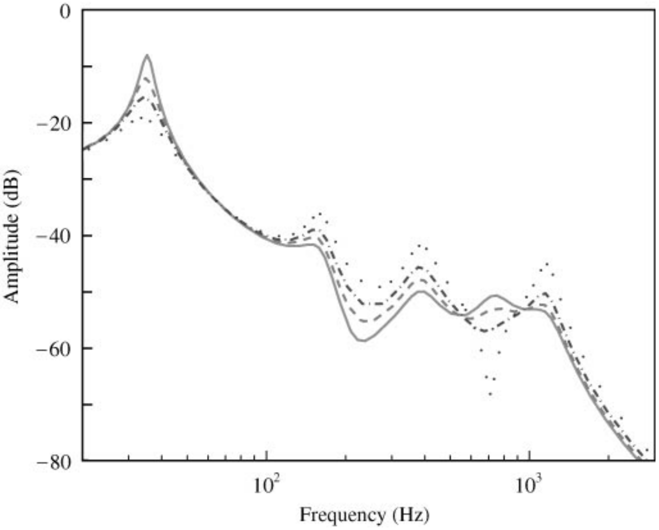

Figure 12. Open- and closed-loop FRF of the sandwich beam, measured by the piezoelectric sensor voltage and loaded by the perturbation transverse force, for three velocity feedback control gains. K_d values: —, 0; - - -, 137; · – · –, 302; ······, 605.

TABLE 3

Modal damping factors (%) for $\dot{w}_L$ and $\dot{V}_S$ feedback at maximum gain

	1	2	3	4	5
Passive	5·2	13·4	16·3	16·0	15·6
Gain $\dot{w}_L$	13·9	− 2·6	− 4·2	7·6	− 7·3
Gain $\dot{V}_S$	16·7	2·4	4·8	4·5	83·7

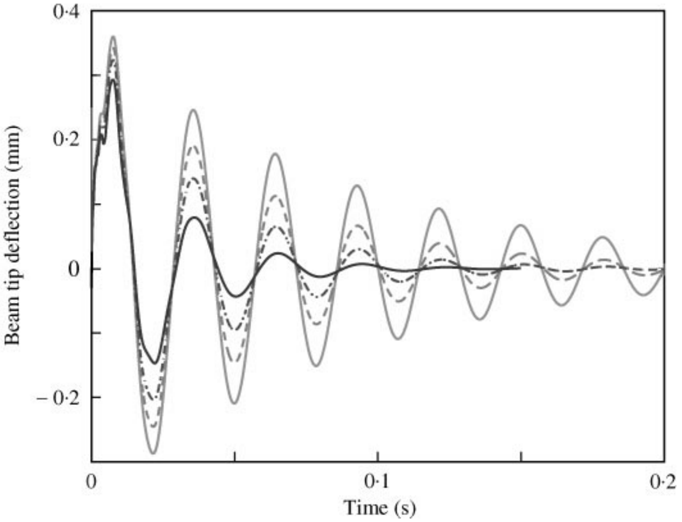

Figure 13. Open- and closed-loop transient responses of the beam tip deflection for three velocity feedback control gains: K_d values: ······, 0; - - -, 137; · − · −, 302; —, 605.

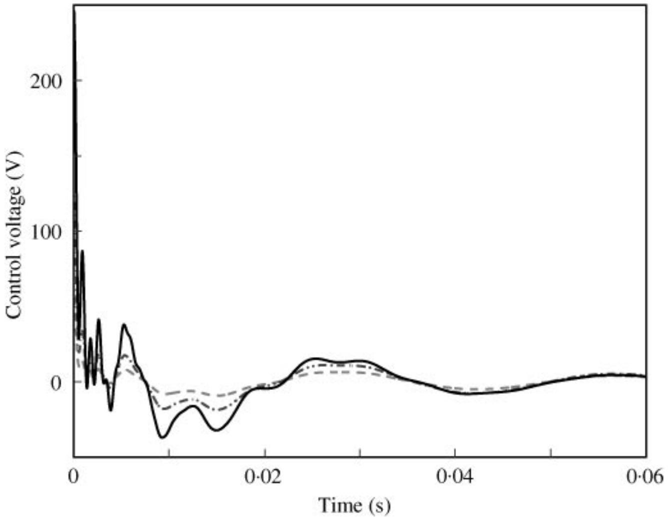

Figure 14. Control voltages imposed to the piezoelectric actuator for three velocity feedback control gains. K_d values: - - -, 137; · − · −, 302; —, 605.

viscoelastic layer is sufficient to prevent destabilization of these modes, so that their total damping factors are still positive.

The open- and closed-loop time-domain impulsive responses of the beam tip deflection, loaded by the perturbation transverse force, are presented in Figure 13, for the three control gains considered. One notices that the settling time of the transient response of the beam tip decreases with the control gain. For $K_d = 605$, the derivative feedback performances are similar to those obtained with the LQR controller (Figure 9). However, to obtain these performances while respecting the piezoelectric actuator voltage limitation (250 V), the beam tip deflection is limited here to 0·36 mm, that is, 24% of that considered for the LQR controller (1·5 mm). Figure 14 shows the actuator control voltage for each control gain. It

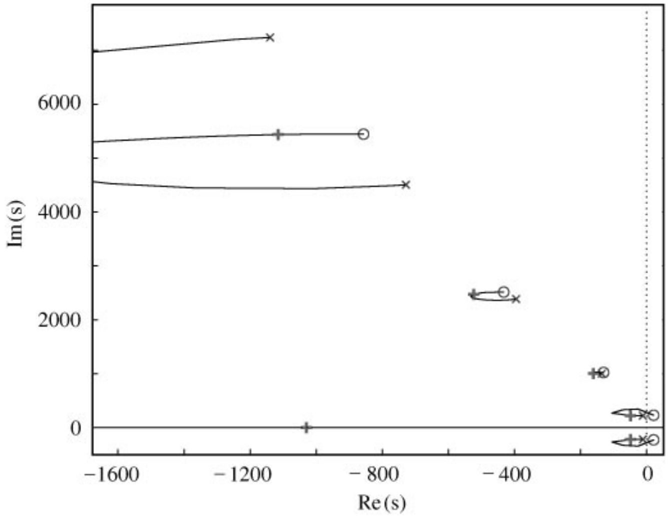

Figure 15. Root locus between the piezoelectric sensor and actuator bonded on the opposite surfaces of the sandwich beam (open-loop poles, ×, and zeros, ○, and closed-loop poles, +, for $K_d = -13{\cdot}5 \times 10^{-3}$).

can be seen that, for $K_d = 605$, the control voltage is, indeed, limited to 250 V. In addition, it presents fast oscillations representing the voltage for actively controlling the fourth mode.

5.2.2. *Sensor voltage rate feedback*

Here, the piezoelectric sensor, bonded on the bottom surface of the sandwich beam (Figure 2), is used in the control loop. In this case, the time derivative of the voltage V_S, induced in the sensor by the beam deflection, is measured, amplified and fed back to the actuator. Consequently, the control voltage is given by $V_A = -K_d \dot{V}_S$. In the previous case, the voltage needed to cancel the first bending mode was opposite to the beam tip deflection, so that a negative-control feedback led to vibration damping. However, in the present case, the beam deflection induces opposite voltages in the piezoelectric patches. Thus, the control gains must be negative. Indeed, the application of a control voltage of the same sign as the sensor voltage leads to a bending cancellation. Figure 15 shows the root locus between the piezoelectric sensor and actuator bonded on the opposite surfaces of the sandwich beam, for control gains varying in the range $[0, -\infty]$. One may notice that all modes are damped for small control gains K_d, whereas for large ones, the first and fifth modes are destabilized. The poles and zeros corresponding to the second mode almost cancel each other, so that damping increase may only be small. The closed-loop poles, +, for the highest control gain $K_d = -13{\cdot}5 \times 10^{-3}$ are also presented in Figure 15. Notice that those corresponding to the fifth mode are in the real axis $\mathrm{Im}(s) = 0$, since this mode is overdamped by the controller.

In Figure 16, the frequency response of the sensor voltage, limited to the first five bending modes, is presented for three control gains $-4{\cdot}5 \times 10^{-3}$, $-9{\cdot}0 \times 10^{-3}$ and $-13{\cdot}5 \times 10^{-3}$. As expected from the analysis of Figure 15, all modal damping is increased. Figure 16 shows that the hybrid controller eliminates the resonance of mode 5 and highly attenuates those of the modes 3 and 4. One may notice that, whereas the controller proportional to the tip velocity improves the first mode in spite of the others, the present one increases all modal damping (Table 3). This may be explained by the evident major contribution of the first mode to the beam tip deflection. This dependence of the damping performance on the relative positions of actuator and sensor is the main disadvantage of the derivative

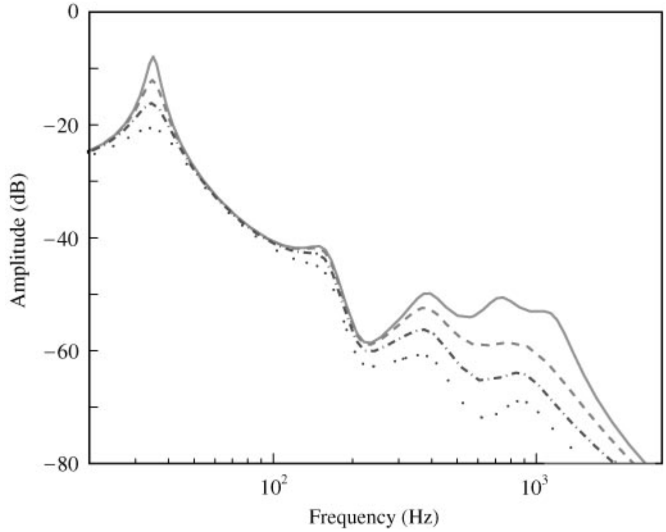

Figure 16. Open- and closed-loop FRF of the sandwich beam, measured by the piezoelectric sensor voltage and loaded by the perturbation transverse force, for three voltage rate feedback control gains. K_d values: —, 0; - - -, − 4·5e − 3; · — · —, − 9·0e − 3; ······, −13·5e − 3.

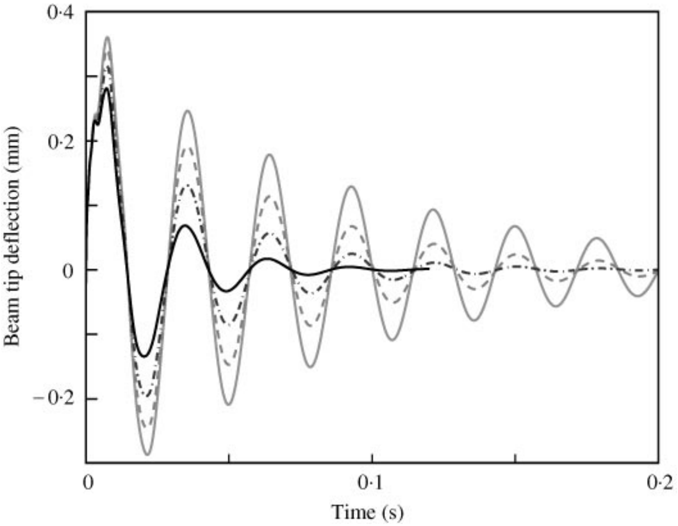

Figure 17. Open- and closed-loop transient responses of the beam tip deflection for three voltage rate feedback control gains. K_d values: ······, 0; - - -, − 4·5e − 3; · — · —, − 9·0e − 3; —, −13·5e − 3.

controllers. In fact, in both cases studied here, the control performance of the first mode is rather limited when compared to that obtained with the LQR algorithm.

The open- and closed-loop time-domain impulsive responses of the beam tip deflection are presented in Figure 17. One notices that the transverse vibrations of the sandwich beam are damped only slightly faster then for the velocity feedback controller (cf., Figure 13). The similarity of the settling performances of Figures 13 and 17 is mainly due to the similarity of the closed-loop damping factors of the first mode for both controllers (Table 3), since the tip response is almost only composed of this mode contributions. Figure 18 shows the control

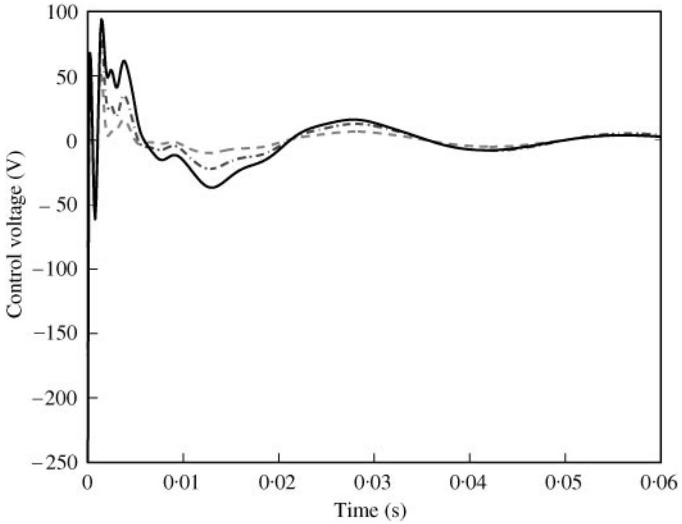

Figure 18. Control voltages imposed to the piezoelectric actuator for three voltage rate feedback control gains. K_d values: - - - - -, − 4·5e − 3; · − · − · −, − 9·0e − 3; ——, −13·5e − 3.

voltages imposed to the piezoelectric actuator for the three control gains. As for the previous case, the voltage is below the limit of 250 V. One can also see, from Figure 18, that the fast oscillations of the control voltage are damped more quickly than for the previous controller. This may be due to the fact that the higher-frequency modes are better damped in this case.

This section has shown that derivative control, although simple to implement, is much less effective than LQR. In addition, for non-collocated sensor and actuator (section 5.2.1), this algorithm leads to a decrease in the damping performance of some modes. Nevertheless, in practical active control design, it is usually difficult to avoid excitation of some modes, due to modelling errors or noise and delay in control electronics. Hence, the destabilization effect of tip deflection velocity feedback shows how the presence of some passive damping is important to prevent total destabilization of the excited modes. On the other hand, although the almost collocated derivative control of section 5.2.2 does not excite the modes considered, it provides also very poor damping performance. This is due to the fact that optimization of the damping of some selected modes is very dependent on the relative actuator/sensor position and the passive damping.

5.3. LQG CONTROL OF THE OPTIMAL BEAM CONFIGURATION

In this section, the optimal full-state observer presented previously (section 4.2) is applied to the control of the sandwich beam of Figure 2 with the optimal parameters $a = 70$ mm and $h_v = 0{\cdot}1$ mm. The interest of considering an LQG controller is to obtain the control parameterization, robustness and performance of LQR while measuring only the output $\mathbf{y}$, instead of all state variables. Since one may design the LQR controller alone and then couple it with a Kalman Filter, the approach of section 5.1 will be used to evaluate the control gain $\mathbf{K}_g$ and then, for given input $\mathbf{W}$ and output $\mathbf{V}$ noise covariances (scalars in this case), system (23) is constructed. The main difficulty introduced by the observer is the coupling between its own dynamics with that of the mechanical system. Moreover, since the initial conditions of all state variables are not known, the initial observer error is $\mathbf{e}(0) = \hat{\mathbf{x}}(0)$. Consequently, as long as the observer error does not disappear the controller

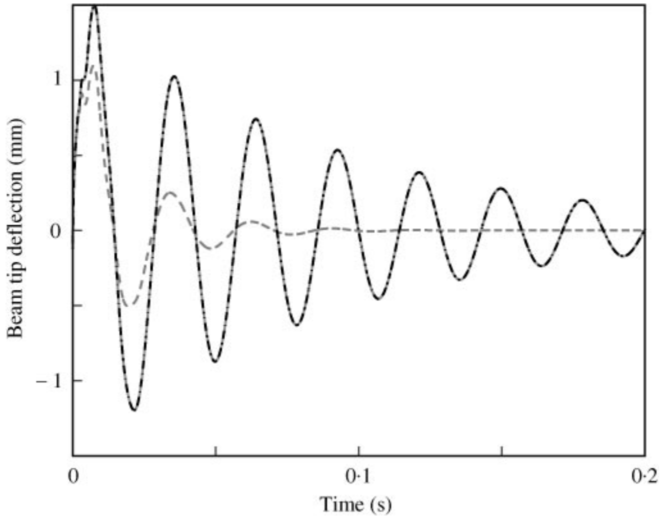

Figure 19. Transient response of the sandwich beam controlled by an LQG with output noise covariance $\mathbf{V}=\mathbf{1}$: —, passive; - - -, hybrid LQR; ·–·–, hybrid LQG.

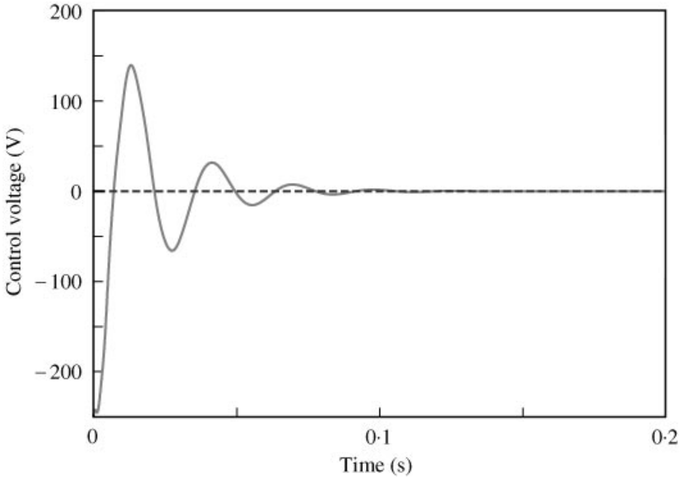

Figure 20. Control voltage for the LQG controller with output noise covariance $\mathbf{V}=\mathbf{1}$: —, LQR; - - -, LQG.

will not be able to control the beam. In the opposite, if the initial state $\hat{\mathbf{x}}(0)$ is known, the initial observer error vanishes ($\mathbf{e}(0)=\mathbf{0}$) and the LQG closed-loop response is equivalent to that of the LQR.

Considering the practical case, where the initial state is unknown, the responses of the system, uncontrolled and controlled by LQR and LQG controllers, are compared for several output noise covariances $\mathbf{V}$. The input noise covariance is fixed to $\mathbf{W}=10^{-5}$. Figures 19 and 20 present the transient output response and control voltage for $\mathbf{V}=1$. Figure 19 shows that the LQG open- and closed-loop responses are the same, meaning that the LQG controller is not effective for this output noise. This may be explained by the fact that, since $\mathbf{V}$ is relatively large, corresponding to a noisy output measure, the observer gain remains small to prevent injection of this noise in the system. Consequently, the observer error is damped more slowly than the LQR closed-loop system. Thus, the LQG control voltage $\mathbf{u}=-\mathbf{K}_g\tilde{\mathbf{x}}=-\mathbf{K}_g(\hat{\mathbf{x}}-\mathbf{e})$ is almost nil, as shown in Figure 20, and does not affect the system.

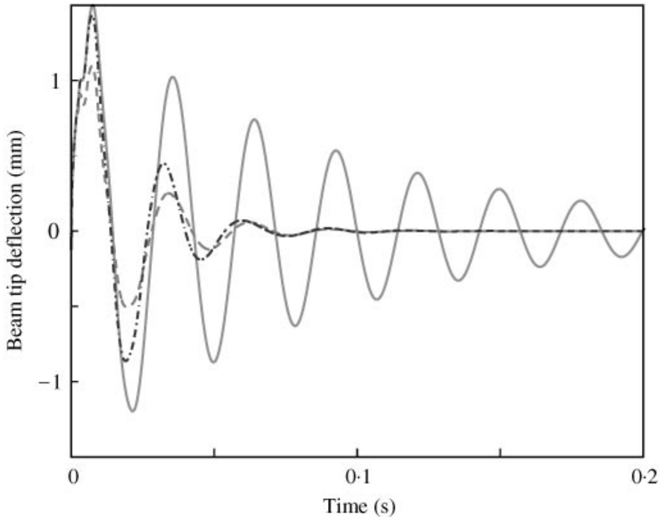

Figure 21. Transient response of the sandwich beam controlled by a LQG with output noise covariance $\mathbf{V} = 10^{-8}$: —, passive; - - -, hybrid LQR; ·—·—, hybrid LQG.

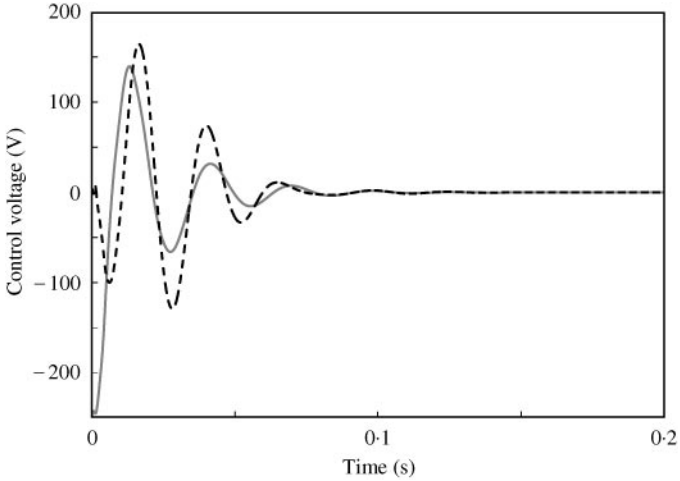

Figure 22. Control voltage for the LQG controller with output noise covariance $\mathbf{V} = 10^{-8}$: —, LQR; - - -, LQG.

Reducing the output noise covariance to $\mathbf{V} = 10^{-8}$, the observer error converges quickly to zero and the state is estimated before being damped, as shown in Figure 21. However, for a performance similar to that of the LQR, the control voltage of the LQG controller is smaller during the initial instants and then larger than that imposed by the LQR one (Figure 22). This is due to the time needed for the observer to well estimate the state and inject it in the control. Hence, as long as the error does not vanish, the estimated state $\tilde{\mathbf{x}}$ is small compared to the real one $\hat{\mathbf{x}}$, such that the control voltage $\mathbf{u} = -\mathbf{K}_g\tilde{\mathbf{x}}$ is also small. Then, $\tilde{\mathbf{x}}$ converges to $\hat{\mathbf{x}}$ and the LQG control voltage increases to damp the system response. This delay effect is quite advantageous in this particular case since the maximum control voltage is reduced (Figure 22) for a similar damping performance.

To accelerate the state estimation, the output noise covariance is reduced to $\mathbf{V} = 10^{-10}$. However, as shown in Figures 23 and 24, although the state estimation is faster, the control performance decreases and the maximum control voltage exceeds the actuator saturation

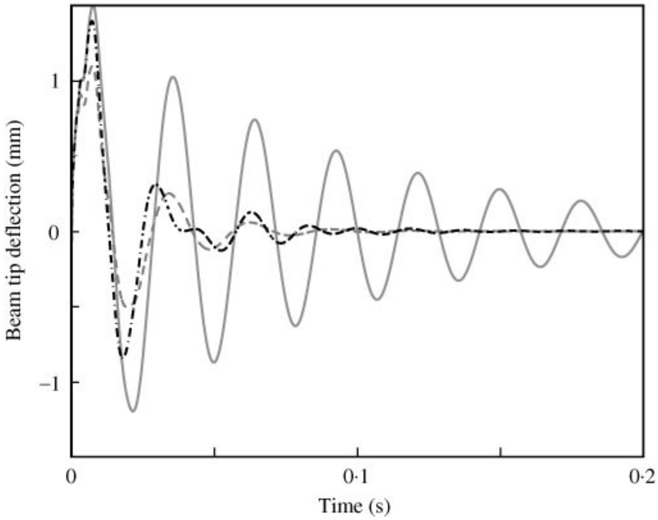

Figure 23. Transient response of the sandwich beam controlled by a LQG with output noise covariance $\mathbf{V} = 10^{-10}$: —, passive; - - -, hybrid LQR; · – · –, hybrid LQG.

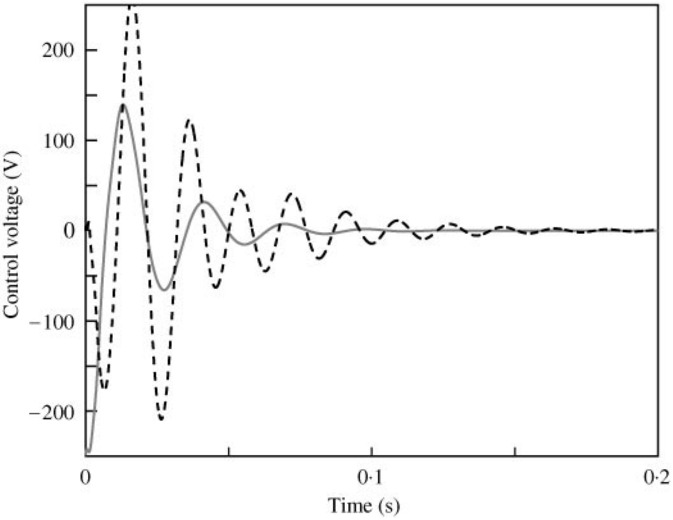

Figure 24. Control voltage for the LQG controller with output noise covariance $\mathbf{V} = 10^{-10}$: —, LQR; - - -, LQG.

voltage of 250 V. In fact, the maximum output amplitude is smaller in this case ($\mathbf{y}_{max} =$ 1·40 mm against $\mathbf{y}_{max} = 1{\cdot}43$ mm for $\mathbf{V} = 10^{-8}$), although still larger than that of the LQR controller ($\mathbf{y}_{max} = 1{\cdot}10$ mm). Nevertheless, the settling time ($t_s = 0{\cdot}14$ s) is higher than that for $\mathbf{V} = 10^{-8}$, which is equal to that of LQR ($t_s = 0{\cdot}12$ s). Moreover, from Figure 24, one notices that the observer excites the structure after estimation. This explains the higher amplitude and settling time of the control voltage. The excessive augmentation of the observer gain may lead to a control system sensitive to less or non-controlled modes. Moreover, additional decrease of the output noise covariance does not improve either the damping performance or the control voltage.

It is clear, from equation (23), that accounting for a state observer increases the system dimension. However, as presented previously, the observer design does not affect the control design, unless the modification of the control voltage induced by the observer is accounted for. Hence, the controller and the observer may be designed separately. For the particular case studied in this section, the LQG controller with $\mathbf{V} = 10^{-8}$ leads to a similar performance with less control voltage than the LQR one. However, it should be noticed that, in practical cases, the output noise covariance is inherent to the signal processing equipment and could not be chosen as a control parameter. Thus, performance as good as for a LQR controller may not always be possible. Moreover, the LQG algorithm did not account for modelling errors, since both observer and controller were based on perfect knowledge of the system dynamics. Alternatively, this could be done using a robust controller as presented in reference [7].

6. CONCLUSIONS

Using a finite-element model able to handle sandwich beams with piezoelectric laminated surface layers and viscoelastic core, the design and analysis of the piezoelectric active control of damped sandwich beams has been presented. The piezoelectric direct and converse effects were represented through additional electrical d.o.f., condensed at the element level. Lesieutre's anelastic displacement fields model was used to represent the frequency dependence of the viscoelastic material properties. This led to an augmented state space system, which was then reduced using a complex modal base that eliminates higher frequencies elastic and overdamped relaxation modes. The complex reduced-order system was then transformed to an equivalent state space real representation to allow system analysis and control. Linear quadratic regulator, linear quadratic Gaussian and derivative feedback algorithms were then applied to the reduced-order model. They were all used in an iterative form to account for maximum control voltage, thus guaranteeing control feasibility and preventing piezoelectric material depoling.

Parametric analyses of the open- and closed-loop damping performances of a cantilever damped sandwich beam with bonded piezoelectric actuator and sensor were performed. Actuator length and viscoelastic core thickness were optimized to yield good passive and hybrid damping performances for the first three bending modes. Results have shown that optimal performances are obtained for long actuators and thin viscoelastic cores. It was also shown that, in the optimal hybrid configuration, the LQR algorithm improves the first modal damping by 400%, while retaining the passive damping of the remaining modes, even uncontrolled ones. Application of a derivative feedback controller to the sandwich beam optimal geometrical configuration has led to less effective damping as compared to the LQR controller. In fact, both tip deflection and sensor voltage derivative feedback controllers were not performant to control the first bending mode, although the latter was able to control other modes. These results have confirmed the dependence of this algorithm performance on the actuator and sensor relative localization. However, the well-known spillover destabilizing effects of derivative feedback controllers were attenuated by the increase of stability margins provided by the viscoelastic damping. In addition, analysis of the effect of an output noise in an LQG full-state optimal observer/controller was performed. It was shown that using the LQG algorithm, the control parameterization, robustness and performance of LQR may be obtained while measuring only the output $\mathbf{y}$, instead of all state variables. Moreover, for the specific case studied in this work, the delay effect induced by the state estimation of LQG was quite advantageous, since a damping performance similar to that of LQR was obtained with a reduced maximum control voltage.

Other hybrid active–passive damping configurations, obtained by several arrangements of piezoelectric and viscoelastic layers, acting conjointly or separately, have been studied and compared but will be presented in a forthcoming paper [14]. Also, other promising control algorithms, such as the PPF and independent modal space control (IMSC), are being considered for active–passive damping treatments.

ACKNOWLEDGMENTS

This research was supported by the "Délégation Générale pour l'Armement", Advanced Materials Branch, under contract D.G.A./D.S.P./S.T.T.C./MA. 97-2530, which is gratefully acknowledged.

REFERENCES

1. D. J. MEAD 1999 *Passive Vibration Control*. New York: John Wiley & Sons.
2. G. A. LESIEUTRE and U. LEE 1996 *Smart Materials and Structures* **5**, 615–627. A finite element for beams having segmented active constrained layers with frequency-dependent viscoelastics.
3. M. A. TRINDADE, A. BENJEDDOU and R. OHAYON 2000 *Journal of Vibration and Acoustics*, **122**, 169–174. Modeling of frequency-dependent viscoelastic materials for active-passive vibration damping.
4. M. I. FRISWELL and D. J. INMAN 1998 in *Smart Materials and Structures* (G. R. Tomlinson and W. A. Bullough, editors), pp. 667–674. Bristol (UK): IoP Publishing. Hybrid damping treatments in thermal environments.
5. M. A. TRINDADE, A. BENJEDDOU and R. OHAYON 2000 *European Journal of Finite Elements* **9**, 89–111. Finite element analysis of frequency- and temperature-dependent hybrid active-passive vibration damping.
6. A. BAZ 1998 *Journal of Sound and Vibration* **211**, 467–480. Robust control of active constrained layer damping.
7. J. CRASSIDIS, A. BAZ and N. WERELEY 2000 *Journal of Vibration Control* **6**, 113–136. H_∞ control of active constrained layer damping.
8. M. J. LAM, D. J. INMAN and W. R. SAUNDERS 1997 *Journal of Intelligent Materials Systems and Structures* **8**, 663–677. Vibration control through passive constrained layer damping and active control.
9. W. H. LIAO and K. W. WANG 1997 *Journal of Sound and Vibration* **207**, 319–334. On the analysis of viscoelastic materials for active constrained layer damping treatments.
10. M. A. TRINDADE, A. BENJEDDOU and R. OHAYON 2001 *International Journal for Numerical Methods in Engineering* **51**, 835–864. Finite element modeling of hybrid active-passive vibration damping of multilayer piezoelectric sandwich beams. Part 1: Formulation and Part 2: System analysis. To appear.
11. A. BENJEDDOU, M. A. TRINDADE and R. OHAYON 1999 *American Institute of Aeronautics and Astronautics Journal* **37**, 378–383. New shear actuated smart structure beam finite element.
12. E. FRIOT and R. BOUC 1996 In *2eme Colloque GDR Vibroacoustique*, LMA, Marseille, pp. 229–248. Contrôle optimal par rétroaction du rayonnement d'une plaque munie de capteurs et d'actionneurs piézo-électriques non colocalisés.
13. A. PREUMONT 1997 *Vibration Control of Active Structures: An Introduction*. Dordrecht, The Netherlands: Kluwer Academic Publishers.
14. M. A. TRINDADE and A. BENJEDDOU 2001 In special issue of *Journal of Vibration and Control*. Hybrid active-passive damping treatments using viscoelastic and piezoelectric materials: review and assessment. To appear.